



Attribution of the December 2013 extreme rainfall over the Pearl River Delta to anthropogenic influences

Rui Zhao^{1,2,3} · Chi-Yung Tam¹ · Sai-Ming Lee⁴

Received: 7 September 2022 / Accepted: 18 June 2023 / Published online: 2 August 2023
© The Author(s), under exclusive licence to Springer-Verlag GmbH Germany, part of Springer Nature 2023

Abstract

During 14 to 17 December 2013, the Pearl River Delta (PRD) in South China received its largest wintertime 4-day precipitation of above 100 mm since 1998, due to strong cold air intrusion. Here we investigate the extent to which such extreme rainfall can be attributed to human activities, by carrying out Weather Research and Forecasting (WRF) model multi-physics integrations at a convection-permitting resolution. The factual WRF runs were conducted using the European Centre for Medium-Range Weather Forecasts (ECMWF) Reanalysis (ERA)-Interim as boundary and initial conditions, and the counterfactual runs by the same ERA-Interim forcing with human influences removed. The latter was deduced by subtracting the Coupled Model Intercomparison Project Phase 5 (CMIP5) historical-natural from the historical run outputs. Results show that the 4-day mean rainfall could increase by 11% for 1.2 K near-surface warming on average under human-induced thermodynamic forcing in relation to humidity changes, whereas it increases by 17% for 2 K warming under all forcing (i.e., including dynamic forcing associated with wind circulation changes), which is nearly the Clausius–Clapeyron rate. Moreover, the former and latter forcing can intensify the 95th percentile daily rainfall by ~ 13% and ~ 19%, respectively, suggesting that human-caused dynamic forcing can further exacerbate the thermodynamic-driven rainfall enhancement in this event. Indeed, there is stronger land-sea thermal contrast with anomalous low-level southerly winds and convergence in coastal South China under all forcing. The frontal system and ascending motion are therefore intensified, resulting in even stronger rain rates than under thermodynamic forcing. Moisture budget analysis reveals that the dynamic component accounts for most of the increase in 4-day mean rainfall while the thermodynamic contribution is negligible under all forcing. Our findings highlight the salient role of dynamic effects on intensifying PRD's extreme rainfall in wintertime.

Keywords Extreme precipitation · Anthropogenic forcing · Event attribution · WRF model · Climate downscaling · Pearl River Delta region

1 Introduction

As the climate warms, many regions of the globe have increasingly suffered from extreme hydrological events with devastating consequences for the environment and social

economy (Duan et al. 2016). Compelling observational evidence indicates substantial changes in the frequency and intensity of extreme precipitation from global to regional scales since the second half of the twentieth century (Alexander et al. 2006; Min et al. 2011; Ma et al. 2015; Fischer and Knutti 2016; Huang et al. 2017; Lu et al. 2021). Globally, variations in extreme precipitation can be attributed to anthropogenic warming in relation to greenhouse gas emissions (Zhang et al. 2013; Trenberth and Zhang 2018; Zhang and Zhou 2019). According to the Clausius–Clapeyron (CC) relation, 1 K surface warming can lead to ~ 7% increase in the saturated water vapor pressure, given that relative humidity remains unchanged (Westra et al. 2014; Santer et al. 2007). Assuming the latter holds, extreme rainfall is therefore expected to be enhanced following the CC

✉ Chi-Yung Tam
Francis.Tam@cuhk.edu.hk

¹ Earth System Science Programme, The Chinese University of Hong Kong, Hong Kong, China

² Key Laboratory of Straits Severe Weather China Meteorological Administration, Fuzhou 350001, Fujian, China

³ Fujian Key Laboratory of Severe Weather, Fujian Institute of Meteorological Sciences, Fuzhou 350001, Fujian, China

⁴ Hong Kong Observatory, Hong Kong, China

relation, which has been corroborated by Lau et al. (2013) using CMIP5 outputs.

Extreme precipitation changes due to human-induced warming are also detected at the regional scale (Pall et al. 2011; Myhre et al. 2019; Kirchmeier-Young and Zhang 2020). Many numerical studies on event attribution have been conducted to quantitatively assess how much human activities affect extreme events (Frame et al. 2020; Wang et al. 2018), and to estimate future risks of the occurrence of those extremes (Pall et al. 2011; Burke et al. 2016; Li et al. 2018a). For instance, the attribution analysis of European rainfall extremes using CMIP6 global models pointed to a latitudinal increase in rainfall intensity due to human influences, with increments of 8%, 26%, and up to 41% in the low, mid, and high latitudes, respectively (Tabari et al. 2020); results from a high-resolution regional model illustrate that anthropogenic warming could have increased Hurricane Harvey's extreme precipitation in Texas by ~20% (Wang et al. 2018), with comparable changes found using different models (van Oldenborgh et al. 2018). In China, human forcing has increased the probability of May 2015 extreme rainfall in the south by at least 23% (Burke et al. 2016); the attribution of another exceptional heavy rainfall event in the Yangtze River basin in May 2016 shows a 40% increase in its likelihood. On average, the intensity of extreme rainfall in China increases at near CC rates based on CMIP5 models (Li et al. 2017). However, such rainfall changes over China were not detected using different models and attribution procedures (Li et al. 2018b), which calls for more research into the attribution of precipitation extremes in China.

There are also reports of extreme precipitation increasing (based on surface temperature) at super CC rates (Lenderink and van Meijgaard 2008; Lenderink et al. 2011, 2017; Chen et al. 2021; Zhao et al. 2022). It is proposed that dynamic effects due to human activities may further exacerbate those extremes, i.e., even stronger amplification than pure thermodynamic forcing (Nie et al. 2018; Pfahl et al. 2017; Ali and Mishra 2018). Other studies indicate that moisture-related thermodynamic variations lead to rather homogeneous heavy rainfall increase, whereas dynamic variations due to wind circulation have little (or negative) contribution at a global scale but modulate regional rainfall extremes (Seager et al. 2010; Chou and Lan 2012; Pfahl et al. 2017; Norris et al. 2019). For instance, the dynamic contribution ($9\% \text{ K}^{-1}$) to sub-daily extreme rainfall increase in India is higher than the thermodynamic effect ($6\% \text{ K}^{-1}$) (Ali and Mishra 2018). In addition, human-influenced temperature gradients can modify frontal activities and related precipitation (Kim and Kim 2020).

Under a warming climate, the Pearl River Delta (PRD) region has experienced dramatic increases in heavy rainfall over the last several decades (Lenderink et al. 2011; Sun and

Ao 2013; Fu et al. 2013). There are a few attribution analyses using global climate models (Burke et al. 2016; Li et al. 2018b); however, large uncertainty exists due to their coarse resolutions (Shepherd 2014). Moreover, the physical mechanisms by which how human activities affect PRD extremes remain unclear. In this study, we focus on a wintertime record-breaking rainstorm on 14–17 December 2013, with the use of a convection-permitting regional model, seeking to (1) investigate the extent to which extreme rainfall can be attributed to human activities, and (2) better understand the mechanisms for human-caused precipitation changes, in particular the role of dynamic and thermodynamic effects. The remaining parts of this work are as follows. Section 2 introduces the datasets and approaches used, model description and experimental design, and also the synoptic background of this event. Section 3 elaborates on the event attribution analysis and possible mechanisms, followed by conclusions and discussion in Sect. 4.

2 Data and methodology

2.1 Datasets used

Gridded data of daily precipitation taken from the Climate Prediction Center (CPC) unified precipitation project, available at a $0.5^\circ \times 0.5^\circ$ grid, and also the 3-hourly precipitation dataset from the Tropical Rainfall Measuring Mission (TRMM) 3B42V7 (Huffman et al. 2007), with a spatial resolution of $0.25^\circ \times 0.25^\circ$, are utilized for the WRF-simulated rainfall evaluation. The 6-hourly $0.75^\circ \times 0.75^\circ$ ERA-Interim data are used to drive the regional model for the attribution analyses (Dee et al. 2011). Surface air temperature over land from the Climatic Research Unit (CRU) Time Series (TS) and HadISST global sea surface temperature (SST) are used for comparison with the CMIP5-simulated temperature.

2.2 Overview of the wintertime extreme rainstorm

In the period of December 14–17, 2013, extremely heavy rainfall affected the Guangdong Province with more than 100 mm day^{-1} averaged over the entire PRD. It resulted in the largest 4-day cumulative rainfall for the November-to-January season since 1998 (Fig. S1). Figure 1 shows the 4-day composite maps of wind circulation, wind divergence, and geopotential height at different pressure levels. In the upper troposphere (Fig. 1a), there was an intense westerly jet from North Africa to Southeast Asia and extending into the North Pacific. Disturbances within such a Rossby waveguide were found to be responsible for the initiation of this event (Huang et al. 2019; Li and Sun 2015). In the middle troposphere (Fig. 1b), a deep low was located over the northwest of Russia, accompanied by northerly winds that brought cold

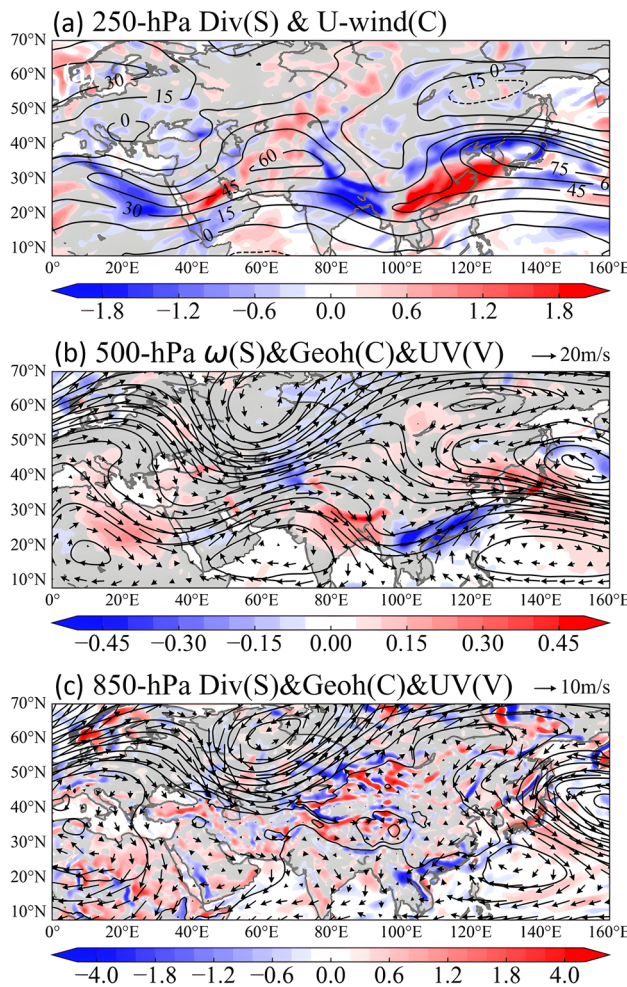
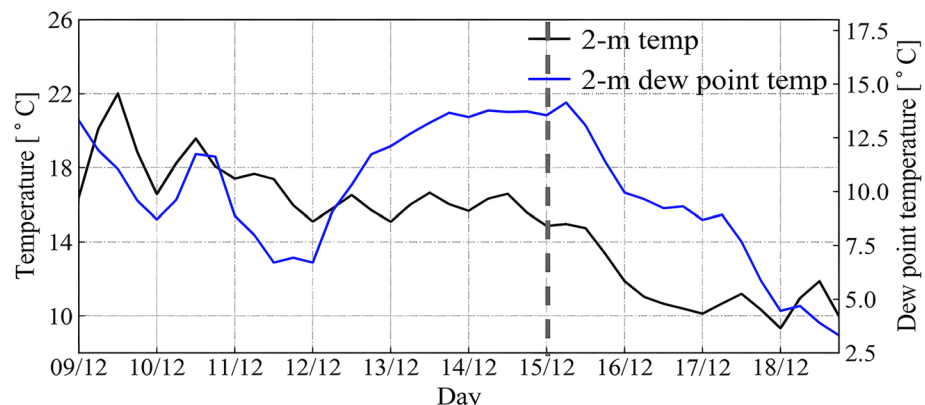


Fig. 1 Composite patterns: **a** 250-hPa wind divergence (shading, units: 10^{-5} s^{-1}) and zonal wind (contours, units: m s^{-1}), **b** 500-hPa vertical velocity (shading, units: Pa s^{-1}), geopotential height (black contours, units: m), and horizontal winds (vectors; see the scale at top right in units of m s^{-1}), **c** 850-hPa wind divergence (shading), geopotential height (black contours), and horizontal winds (vectors; see the scale at the top right in units of m s^{-1}) averaged for December 14–17, based on ERA-Interim data

Fig. 2 Time evolution of 6-hourly air temperature (black, units: $^{\circ}\text{C}$) and 2-m dewpoint temperature (blue, units: $^{\circ}\text{C}$) averaged over the PRD region from December 9 to 18, based on ERA-Interim data



air to the mid-latitudes. A ridge lying over the northeastern Tibet Plateau and a trough over the western Indochina Peninsula further facilitated the southward transport of cold and dry air (see contours in Fig. 1b). Such airflow is seen to converge with southwesterlies (see vectors in Fig. 1b) in South China (SC), accompanied by rising motion at 500 hPa. In the low levels (Fig. 1c), a subtropical high persisted over the western Pacific, transporting warm moist air mainly from the South China Sea (SCS) to SC (Huang et al. 2018). The low-level convergence coupled with the upper-level divergence is consistent with strong atmospheric convection and heavy precipitation (see shadings in Fig. 1c). Cold and dry air invaded the PRD region on December 15, causing a sudden drop in dewpoint temperature of around 10°C by December 17 (Fig. 2). According to the Hong Kong Observatory records, the surface temperature reached the annual minimum of 9.2°C on December 18.

2.3 Methods, model setup, and experiment design

To eliminate the CMIP5 projections that are unable to mimic historical warming, we first evaluated decadal trends of surface air temperature (SAT) averaged over SC for the 1901–2005 period, using the variables “tas” in historical runs of 18 CMIP5 global climate models (GCMs) against the observed trend using CRU TS data (Fig. S2); ten models with comparable SAT trends were initially selected (highlighted with the blue background in Fig. S2). Then we compared the SAT time series between historical and historical-natural runs of each model; seven out of ten CMIP5 models that have noticeable difference between two runs since 1980 were finally employed in order to obtain robust anthropogenic signals (Fig. S3). Detailed information of the selected models is given in Table S1.

Attribution experiments were carried out using the Advanced Research WRF (WRF-ARM) model version 3.8.1 (Skamarock et al. 2008). Figure 3 shows the three nested domains centered on the PRD region, with the outermost domain (79×61 grid cells) having a grid spacing of

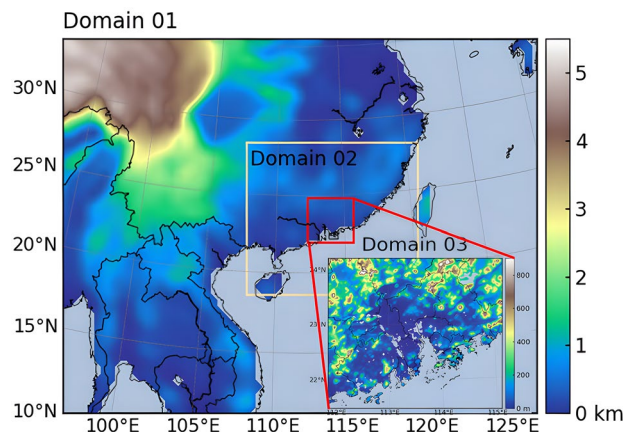


Fig. 3 Spatial distribution of topographic height (units: km) over the three nested domains in WRF

50 km × 50 km, covering most of southeast Asia, the middle and innermost domains encompass the SC and PRD region, with a horizontal resolution of 10 km × 10 km (136 × 116 grid cells) and 2 km × 2 km (181 × 166 grid cells), respectively; one-way nesting was used. To reduce the model bias, 6-member ensemble integrations were conducted by combining different microphysics schemes, i.e., the Thompson microphysics (Thompson et al. 2008) and single-moment six-class (WSM6) microphysics (Hong 2006), and cumulus parameterizations, i.e., the Kain–Fritsch scheme (Kain and Kain 2004), Betts–Miller–Janjic (Janjic 1994) and Grell 3D (Grell and Dévényi 2002) schemes (see Table S2). Cumulus parameterization is turned off in the innermost WRF domain. Other physics packages include the Bougeault–Lacarrere PBL scheme (Bougeault and Lacarrere 1989), the rapid radiative transfer model for both shortwave and long-wave radiation parameterizations (Iacono et al. 2008), and the unified Noah land surface model (Tewari et al. 2004). Zonal and meridional winds above 500 hPa in the outermost domain were spectrally nudged to the corresponding values taken from ERA-Interim, at the scale of about 1300 km (1500 km) in the zonal (meridional) direction (Liu et al. 2012; Ma et al. 2016; Fung et al. 2021).

Three sets of WRF runs were designed to attribute heavy rainfall changes to human impacts by dynamically downscaling the event under different initial and boundary conditions (IBCs) over the period from 0000 UTC 9 December to 0000 UTC 18 December 2013, with the first 48 h being excluded as spin-up effects. In the control run (CTL), the model was forced with IBCs from ERA-Interim, which represents the factual climate that includes both anthropogenic and natural forcings. In two counterfactual runs, IBCs are derived by removing (1) human-induced thermodynamic (i.e., temperature and specific humidity) perturbations (hereafter DTQ run), and (2) both human-related thermodynamic and

dynamic (i.e., horizontal wind circulation) perturbations (hereafter DTQW run) from ERA-Interim. Hence, human-forced thermodynamic and dynamic variations that affect heavy rainfall can be inferred from the difference between CTL and DTQ runs, as well as DTQ and DTQW runs. The perturbed fields were computed as the monthly averages of the thirty-year (1986–2005) mean differences between historical and historical Nat runs of the seven-model averaged CMIP5 ensemble mean. The use of a multi-model mean can minimize the model uncertainty and internal climate variability from individual CMIP5 models (Liu et al. 2017). Recall that such an ensemble mean underestimates the observed SAT trend. We hence rescaled the CMIP5 perturbations, based on the ratio of the observed to the seven-model mean SAT trend. The adjusted monthly perturbations were then interpolated linearly on each model grid in the outermost domain.

3 Results

3.1 Model evaluation of the event

We first evaluate the spatial–temporal distribution of simulated rainfall during this event based on satellite and rain gauge observations. Figure 4 depicts the daily precipitation averaged from December 14 to 17 over SC, from the WRF CTL runs using different physics schemes, TRMM 3B42 products and gauge-based CPC observations. In general, the multi-physics ensemble-mean CTL simulation agrees better with observations (especially TRMM 3B42) than simulations from individual schemes, in terms of both pattern and intensity of the rainband. Both WG3 and WKF schemes overestimate the rain rates. TBMJ is comparable to CPC but less than TRMM-observed rainfall; however, the simulated rainband is shifted to the northwest by ~110 km. Shen and Xiong (2016) pointed out CPC tends to smooth out precipitation structures and underestimates rainfall intensity over Mainland China. It is also noteworthy that the WRF-simulated daily precipitation evolution in PRD matches closely the observed (Fig. 5). The model gives maximum rainfall on December 15 and 16 of 40 mm day⁻¹ or more, with a slight underestimation of the mean rainfall when compared with CPC data (see numbers in brackets in Fig. 5).

Model's performance in reproducing meteorological variables such as specific humidity, horizontal wind and vertical velocity, during this extreme rainfall process are also assessed using ERA-Interim data (Fig. S4). The model successfully captured the evolution of specific humidity, with maximum values of ~10 g kg⁻¹ below 800 hPa from December 14 to 15 (Fig. S4a, b). However, humidity is underestimated prior to the rainfall onset but overestimated on December 16. The simulated wind evolution, especially for

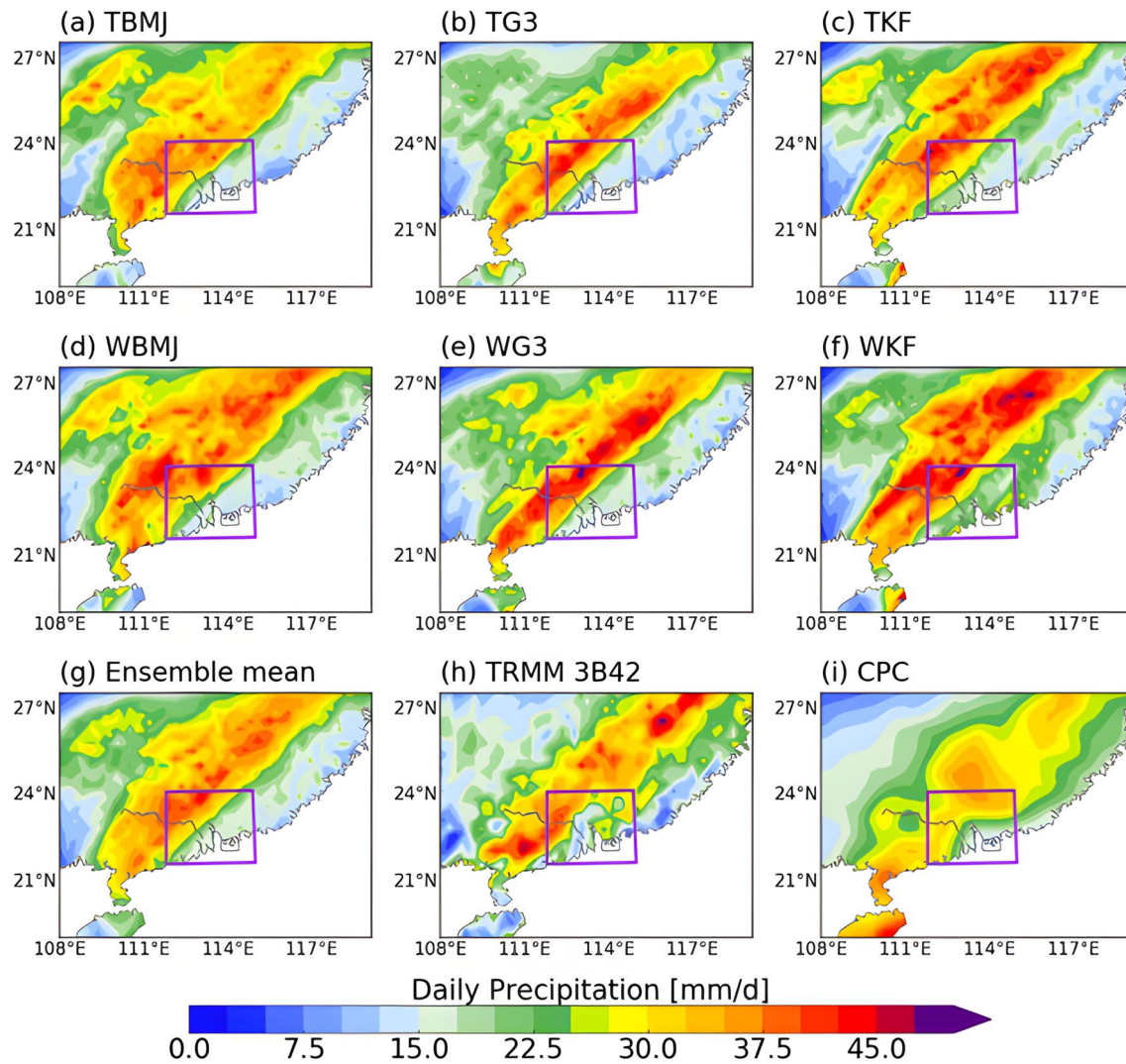


Fig. 4 Daily mean precipitation (units: mm day^{-1}) between December 14 and 17 over South China, obtained from the WRF control runs using **a** Thompson-BMJ, **b** Thompson-Grell 3D, **c** Thompson-KF, **d** WSM6-BMJ, **e** WSM6-Grell 3D, **f** WSM6-KF schemes and **g**

the ensemble mean of the multi-physics members, as well as from **h** TRMM 3B42 product, and **i** gauge-based CPC observations. The purple box in each panel outlines the PRD region

the zonal wind, is in good agreement with observations (Fig. S4c–f). Compared with ERA-Interim, the model reproduced weaker mid-to-upper-level (above 600 hPa) southerly winds, and low-level (below 700 hPa) northerly winds over PRD from December 14 to 17. The observed main ascend (negative) centers on December 15 and 16 were well simulated, although the model gave slightly stronger low-level (below 800 hPa) upward motion during the rainfall period (Fig. S4g, h). Overall, the multi-physics WRF ensemble mean can capture the precipitation pattern and evolution, as well as the associated atmospheric fields of this event.

Furthermore, we evaluated WRF's ability to replicate anthropogenic forcing over the outermost (coarsest resolution) domain as given by the CMIP5 GCMs. From CMIP5 projections (left panels in Fig. 6) human activities have

caused temperatures in December to rise from ~1 K near the surface to around 2 K in the upper levels (above 300 hPa); in low latitudes there tends to be greater vertical temperature gradient in the troposphere than in the mid latitudes (Fig. 6a). The specific humidity increased with warming, reaching the largest values of approximately 0.8 g kg^{-1} in low-level tropics (Fig. 6c). These anomalies are consistent with changes under increased CO_2 warming from the 33 CMIP5 model mean (Lau and Kim 2015). In December there are strong upper-level westerly anomalies due to increased temperature gradient, while weaker zonal winds are found below 300 hPa, particularly at $20\text{--}30^\circ \text{N}$ (Fig. 6e); meridional winds are also strengthened (Fig. 6g). These human-forced temperature and humidity anomalies were removed from variables in IBCs in the WRF DTQ experiments, and

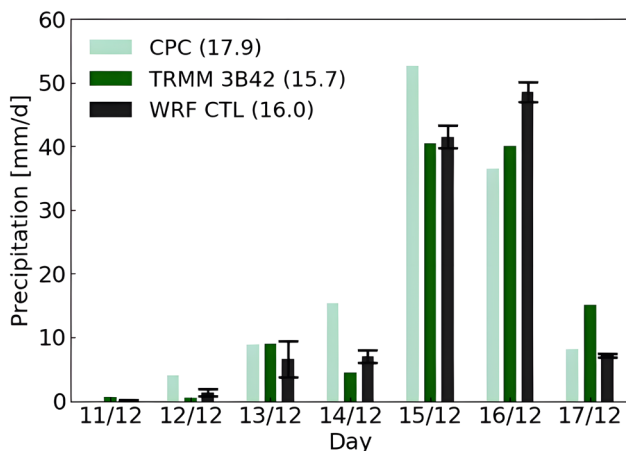


Fig. 5 Time evolution of daily precipitation over the PRD, obtained from rain gauge-based CPC observations (light green), satellite-based TRMM 3B42 product (dark green), and WRF CTL simulations (black). Error bars indicate the standard deviation among the six ensemble members with different physics schemes. Numbers in brackets are the 4-day mean precipitation between December 14 and 17

anomalous wind circulations (in addition to temperature and humidity) were removed in DTQW. Differences between the control and two perturbed WRF runs can therefore be attributed to human impacts on the extreme event. By comparing with CMIP5 ensemble, the WRF model reproduced temperature and humidity anomalies reasonably well (Fig. 6b, d); the vertical profiles of horizontal wind anomalies were also replicated in general (Fig. 6f, h), albeit with stronger westerlies and meridional winds in mid-latitudes (30° N– 34° N).

3.2 Attribution of heavy rainfall to anthropogenic influences

The sensitivity of precipitation to anthropogenic forcing is now examined by comparing rainfall from the control with the counterfactual experiments. We first focus on spatial distribution of the December 14 to 17 average precipitation (Fig. 7), based on the multi-physics ensemble mean. CTL shows rainfall mainly occurred over the northwestern locations in the model domain, accompanied by strong low-level southeasterly winds that facilitate moisture transport from SCS to inland PRD (Fig. 7a). Rain rates in CTL can reach 45 mm day^{-1} within the rainband, which are reduced by 7–10% in DTQ and 13–15% in DTQW (Fig. 7d, e), associated with at least 0.9 K near-surface temperature difference (Fig. 6b). This is broadly consistent with the CC relation, i.e., $\sim 7\%$ moisture increase per degree K of warming (Allen and Ingram 2002; Trenberth et al. 2015). Precipitation over coastal PRD was also suppressed in two perturbed runs, showing a minor reduction of less than 5% in DTQ and a 7–14% decrease in DTQW; the larger reduction in DTQW

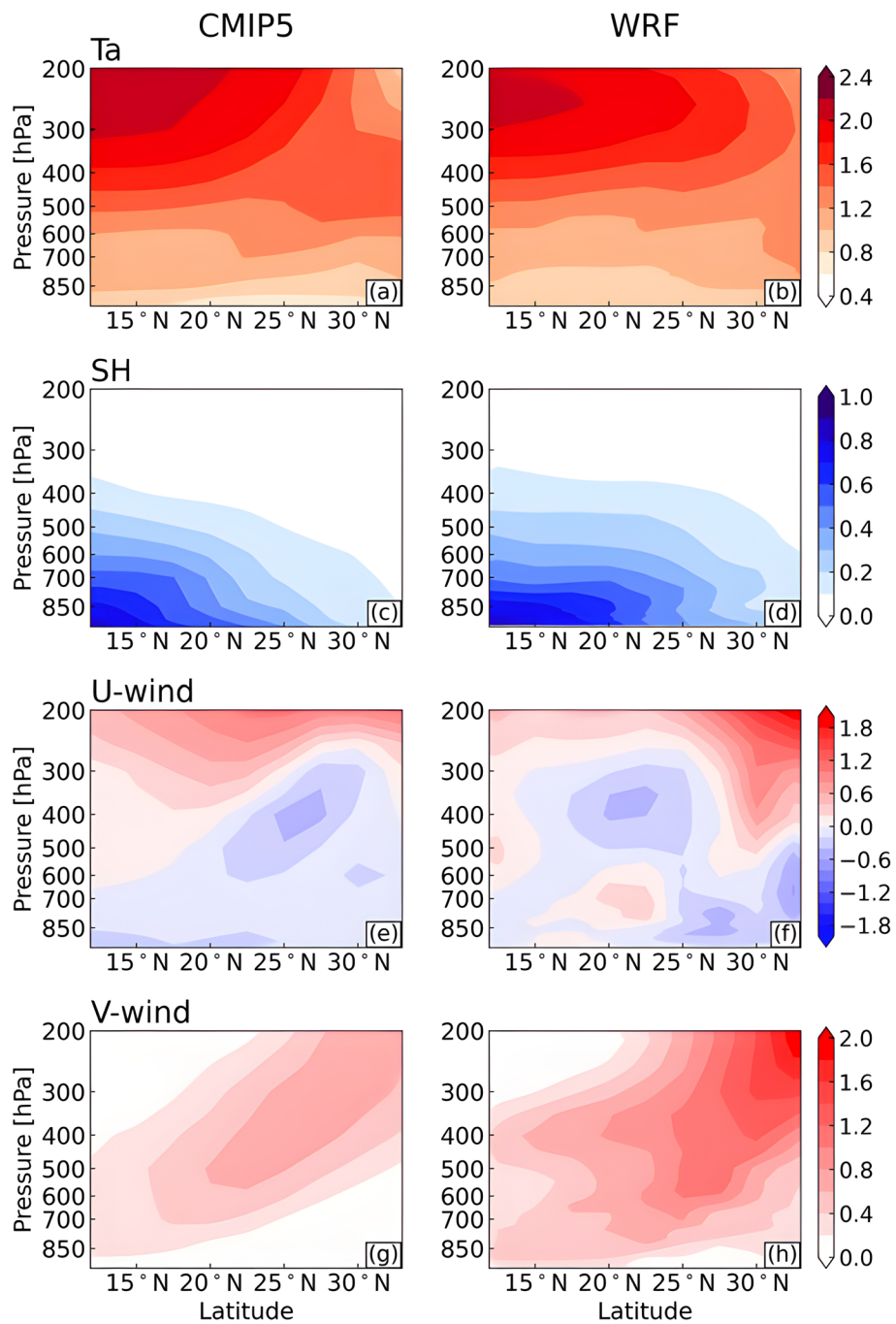
mainly occurred over the cities of Zhongshan (113.4° E, 22.5° N) and Zhuhai (113.6° E, 22.3° N). In contrast, precipitation occurred between the rainband and coastal areas was intensified by 3% at most in DTQ and DTQW when compared with that in CTL, which is likely related to the northward shift of the rainband due to anomalous southerly winds. Overall, the daily mean precipitation in PRD tends to be more intense under a human-induced warming environment. Furthermore, CTL–DTQW shows a larger increase in rainfall intensity than CTL–DTQ, accompanied by anomalous southerly winds that can deliver more moisture to the rainfall locations (see vectors in Fig. 7e).

Here we also assess the PRD daily rainfall time series from the control and counterfactual runs (Fig. 8). Compared to CTL, daily rain rates decrease in both DTQ and DTQW runs on each day of the rainfall period. The reductions are apparently larger than the difference among ensemble members. It is clear that daily rainfall was intensified as a result of the human-induced warmer and wetter background climate; rainfall could become even stronger due to human-induced wind anomalies, in addition to thermodynamic changes.

To quantify such precipitation variations attributable to anthropogenic influences, we calculated the rate of change in daily rainfall with respect to near-surface temperature for each model grid over PRD. The frequency or probability distribution of these gridded rain rates during the rainfall period is given in Fig. 9. Here the change for, say DTQ (red line in Fig. 9), was computed from the relative change in rainfall, i.e., $(\text{CTL} - \text{DTQ})/\text{DTQ}$, divided by the 2-m temperature difference of CTL–DTQ. The same computation was done for the DTQW run. Unanimously in the perturbed runs, the derivatives peak at $10\% \text{ K}^{-1}$, which slightly exceeds the CC scaling of $7\% \text{ K}^{-1}$. There also seems to be a bimodal distribution in DTQW, with a secondary peak at $\sim 36\% \text{ K}^{-1}$.

We further quantified the 4-day mean and extreme precipitation changes of rainfall in CTL relative to DTQ and DTQW, as shown in a box and whisker diagram (Fig. 10). The 4-day average rainfall in CTL was 11% larger than DTQ with an interquartile range from 8 to 14%, and 17% relative to DTQW with a range of 15–20%. For changes in extreme rainfall, i.e., the 95th and 99th percentiles, there is a 13% increase relative to DTQ with a spread of 10–17%, and 19% and 21% increases for 95th and 99th percentiles compared to DTQW, with wider interquartile ranges of 10–18% and 10–32%, respectively. In other words, human-forced thermodynamic effects contribute to at least an 11% rainfall increase, with combined thermodynamic and dynamic forcing resulting in larger increments for both mean and extreme precipitation for this event. Consistent with previous studies, extreme rainfall increase is more robust than that in the daily mean (Alexander et al. 2006; Myhre et al. 2019). Besides, the fractional change of CTL to DTQW shows a large increase in the 99th percentile

Fig. 6 Latitude-height cross-section of human-forced anomalies for **a**, **b** air temperature (units: K), **c**, **d** specific humidity (units: g kg^{-1}), **e**, **f** zonal wind (units: m s^{-1}), and **g**, **h** meridional wind (units: m s^{-1}) averaged between $97\text{--}127^\circ\text{E}$ (outermost domain in WRF). The left panels are derived from the mean difference in December of 1986–2005 between historical and historical Nat runs from CMIP5 seven-model ensemble (see Table S1). The right panels are the difference between WRF control and perturbed runs (i.e., CTL–DTQW) averaged over the case period. See text for details



than the 95th percentile rainfall, suggesting that human-caused dynamic anomalies could intensify very extreme rainfall even further. It is also noteworthy that variations in these extremes can exceed the CC scaling; super-CC behavior was also reported for hourly rainfall changes (Lenderink et al. 2011; Westra et al. 2014). Such additional intensification in both the daily mean and extreme precipitation suggests the important role played by the dynamic effect (Nie et al. 2018).

3.3 Physical mechanisms

3.3.1 Large-scale circulation changes

It has been shown that dynamic effects associated with circulation changes can further exacerbate extreme precipitation due to human forcing. To investigate such dynamic feedback, we first examine human influences on the large-scale temperature, geopotential as well winds structures.

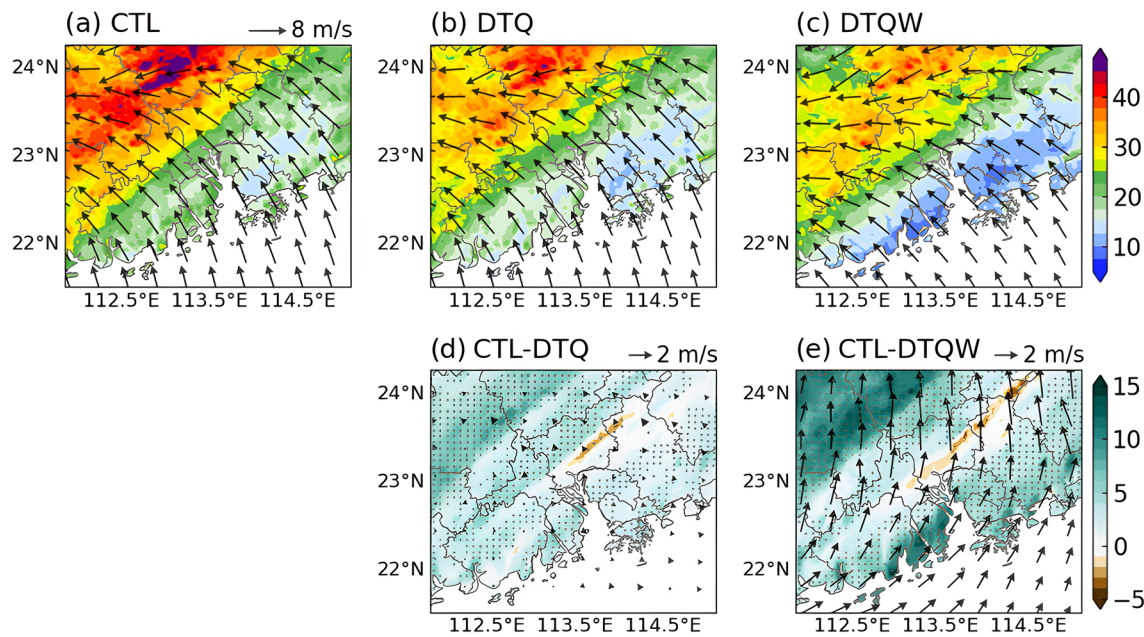


Fig. 7 Daily precipitation (shading, units: mm d^{-1}) overlapped with the 850-hPa horizontal winds (vectors, units: m s^{-1}), averaged from December 14 to 17 over the PRD, from the **a** CTL, **b** DTQ, and **c** DTQW runs, as well as differences between **d** CTL and DTQ, **e** CTL

and DTQW, relative to DTQ and DTQW, respectively. The significant changes in rain intensity at the 90% confidence level based on the Student's *t*-test are marked by grey dots

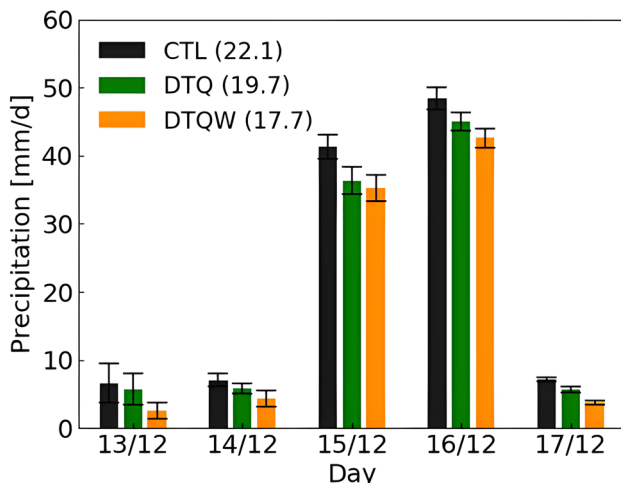


Fig. 8 Time evolution of daily precipitation in the WRF CTL (black bars), DTQ (green bars), and DTQW (orange bars) averaged over PRD. Error bars denote the standard deviation among six ensemble members with different physics schemes

At 850 hPa (Fig. 11), CTL-DTQ warming tends to be stronger in mainland China than in SCS and adjacent continents (Fig. 11b). The enhanced thermal contrast is seen to be accompanied by south-to-southwesterly wind anomalies over the coastal SC in CTL-DTQW (see vectors in Fig. 11f). Meanwhile, warmer central compared to northern parts of SC is associated with anomalous northerly

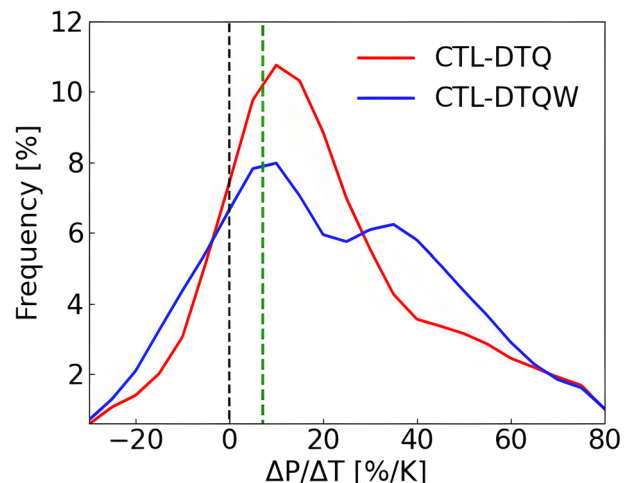


Fig. 9 Frequency distribution of percentage changes in the daily precipitation per degree of 2-m temperature increases on each model grid over PRD for December 14–17, from CTL relative to DTQ (red) and DTQW (blue). The green dashed line indicates the CC scaling of $7\% \text{ K}^{-1}$

winds; thus the regional winter monsoon flow is strengthened. These two airflows converged over the anomalous low over SC (see shading in Fig. 11f), enhancing low-level wind convergence there (see vectors in Fig. 11f). Besides, CTL-DTQW shows stronger warming over PRD inland, which is likely related to urbanization effects (Zhong et al.

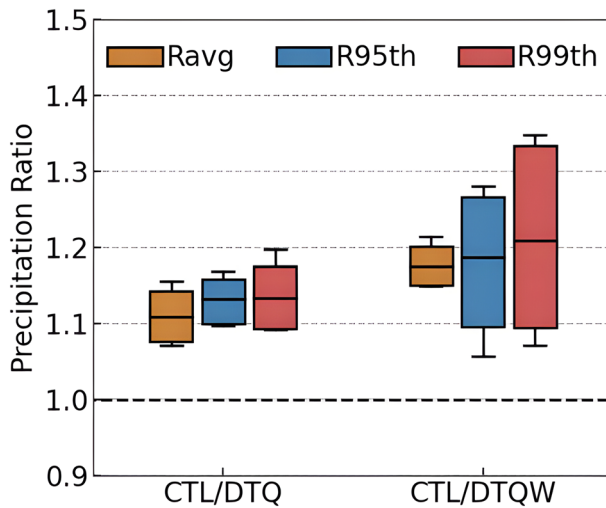


Fig. 10 Box and whisker plot of ratios of the simulated 4-day mean (brown bars), 95th (blue bars), and 99th percentile (red bars) of daily precipitation (units: mm day^{-1}) averaged over December 14–17 in PRD, in the CTL run relative to the DTQ and DTQW runs

2017), and supports anomalous southerlies (Fig. 11c). At 500 hPa, accompanied by anomalous southerly winds (see vectors in Fig. 12f), there is stronger warming over land (especially in central SC) than ocean in CTL–DTQW (Fig. 12c). This anomalous temperature gradient, however,

is not seen in CTL–DTQ (Fig. 12b). The low-level anthropogenic warming also results in higher geopotential at 500 hPa in CTL, with a larger increase over SC when compared to DTQW than DTQ (see shading in Fig. 12e, f); this gives rise to anomalous anticyclonic winds over ESC in CTL–DTQW. Unlike low-level warming, the upper-level (250 hPa) temperature in CTL increases more robustly in low latitudes (south of 19° N) than the subtropics, compared to DTQ (Fig. 13b). In contrast, CTL–DTQW has no distinct warming gradient (Fig. 13c); it also shows the anomalous high pressure over SC with stronger southerlies (Fig. 13f), consistent with temperature changes below 250 hPa.

Changes in wind divergences at 250 hPa and 850 hPa are also examined and presented in Fig. 14. CTL patterns indicate that the low-level wind convergence center covers the PRD region and upper-level divergence appears over the SC, suggesting strong vertical motion (Fig. 14a, d). Such low-level wind convergences over the PRD were greatly intensified compared to DTQW due to human influences (Fig. 14f). On the other hand, human activities have little impact on the upper-level divergence over PRD but intensified the convergence north of PRD (Fig. 14c), which is related to wind changes (Fig. 13f). In contrast, CTL–DTQ shows a much smaller difference (Fig. 13b, e), for no horizontal wind anomalies involved in DTQ.

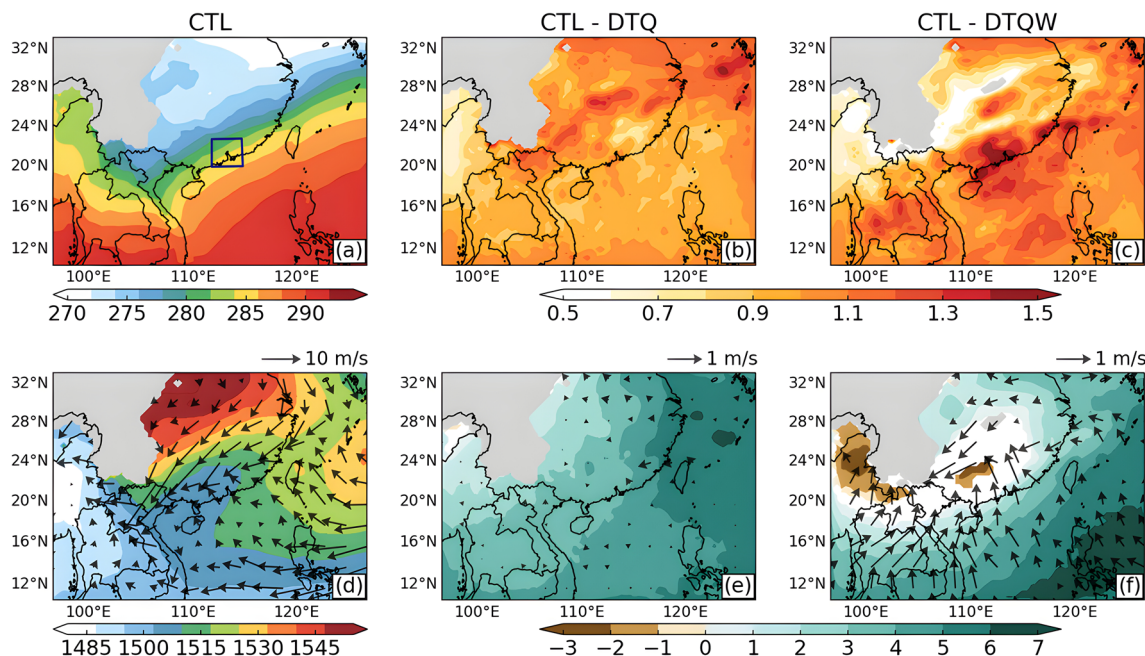


Fig. 11 Composite map of **a–c** the 850-hPa temperature (shading, units: K) and **d–f** geopotential height (shading, units: m) overlapped with horizontal winds at 850 hPa (vectors; see scale arrow at top right in units of m s^{-1}), averaged from Dec 14 to 17 over the outermost domain, in the **a, d** CTL runs, as well as their differences between

b, e CTL and DTQ, **c, f** CTL and DTQW that passed the 90% confidence level based on the Student's *t*-test. Missing values over Tibetan Plateau are masked by grey shading. The dark box in **a** outlines the PRD region

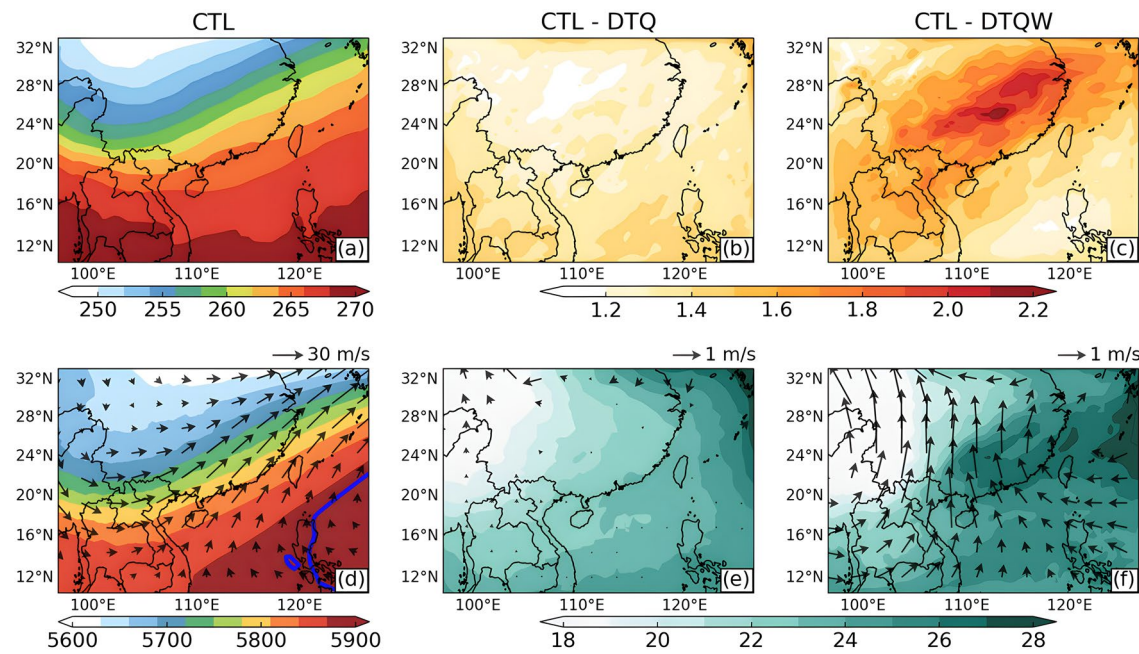


Fig. 12 Same as Fig. 11, but for variables at 500 hPa. The blue thick line denotes the 5880-m geopotential height contour

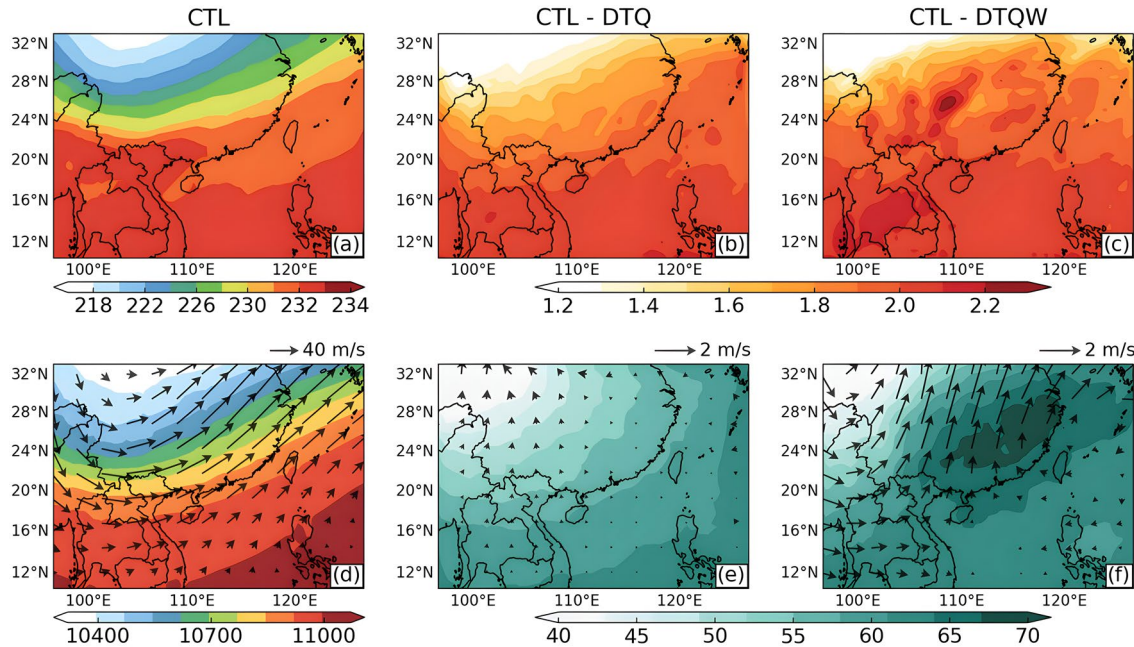


Fig. 13 Same as Fig. 11, but for variables at 250 hPa

3.3.2 Thermodynamic versus dynamic contributions

Next the PRD regional-scale responses of thermodynamic and dynamic effects due to human forcing are inspected. Figure 15 gives the evolution of the induced temperature and specific humidity changes. The difference between CTL and

DTQ indicates that human activities have raised temperature throughout the troposphere, with 1–1.2 K increases in the low levels (below 500 hPa) and 1.5–2 K in the upper troposphere (Fig. 15a). A robust increase in specific humidity is also seen below 700 hPa, peaking at 0.7–1 g kg⁻¹ during the rainfall period (Fig. 15c). However, the difference between

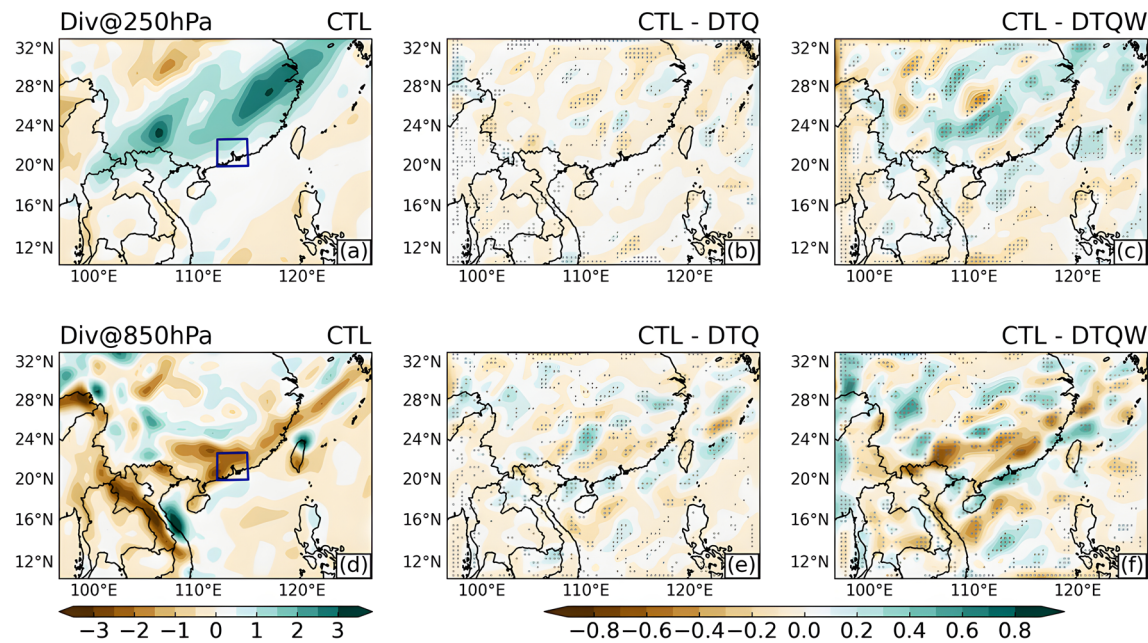


Fig. 14 Composites of divergences (shading, units: 10^{-5} s^{-1}) at **a–c** 250 hPa and **d–f** 850 hPa averaged over Dec 14–17 in the **a, d** CTL runs, and differences between **b, e** CTL and DTQ, **c, f** CTL and

DTQW. Grey dots mark divergence differences at the 90% confidence level based on the Student's *t*-test. Dark boxes in **a, d** outline the PRD region

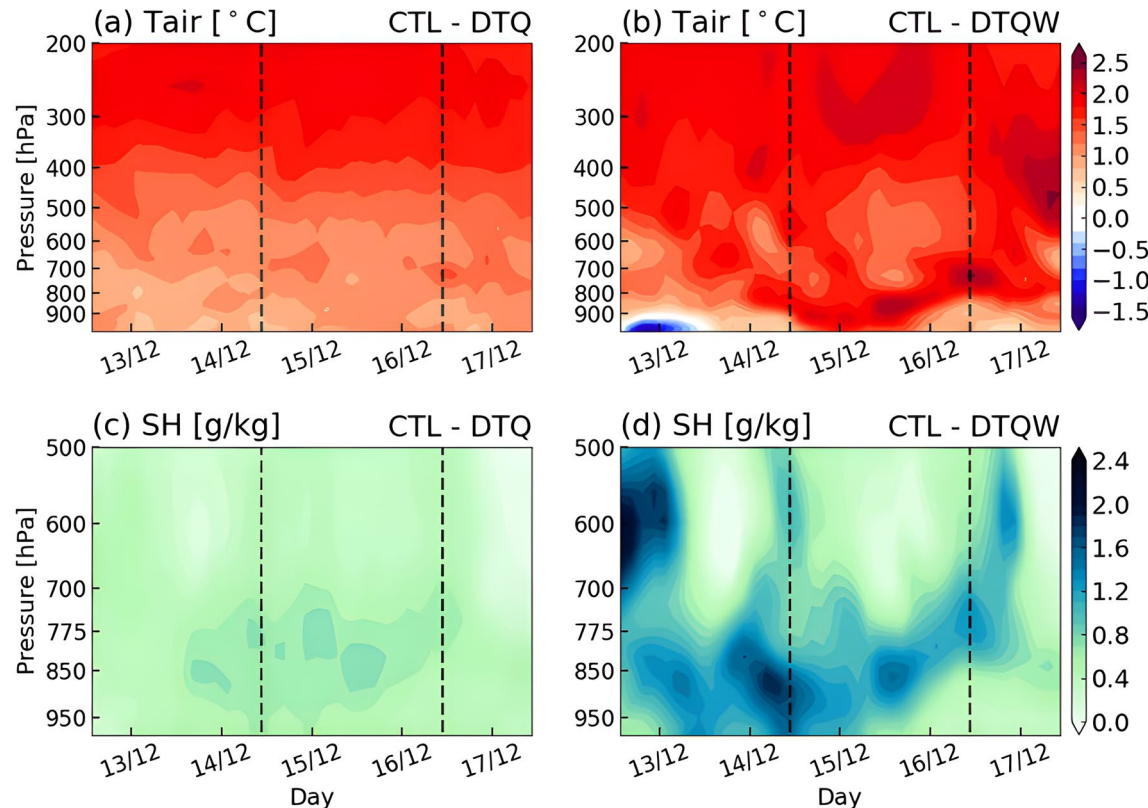


Fig. 15 Time evolution of differences in **a, b** air temperature (units: K) and **c, d** specific humidity (units: g kg^{-1}) averaged over PRD between **a, c** CTL and DTQ run, **b, d** CTL and DTQW run. Black dashed lines indicate the peak rainfall days on December 15 and 16

CTL and DTQW is even more pronounced for both variables. During the peak rainy days, near-surface temperature increases by more than 2 K, and low-level (below 700 hPa) specific humidity rises by about 1.6 g kg^{-1} (Fig. 15b, d). This suggests that additional wind circulation changes could further intensify anthropogenic warming, thus filling a wetter environment in this case.

Human impacts on frontal intensity are investigated based on the meridional gradient of 850-hPa equivalent potential temperature as a parameter (Fig. 16). A larger negative value represents a higher temperature gradient, indicative of more intense cold and dry air intrusion into the PRD region and

thus enhanced frontal intensity. From CTL, a strong cold front approached PRD on December 14 with eastward progression and became strongest on December 15 and 16, during which the rain rate assumed its peak. Compared to CTL, the cold front became weaker in the perturbed runs, with a larger reduction in DTQW than in DTQ, during the whole event period (see black dashed lines in Fig. 16). This clearly shows that the human-influenced wind circulation anomaly can affect temperature changes in turn, altering precipitation characteristics.

We have also inspected the temporal evolution of 850-hPa horizontal wind components, as illustrated in Fig. 17.

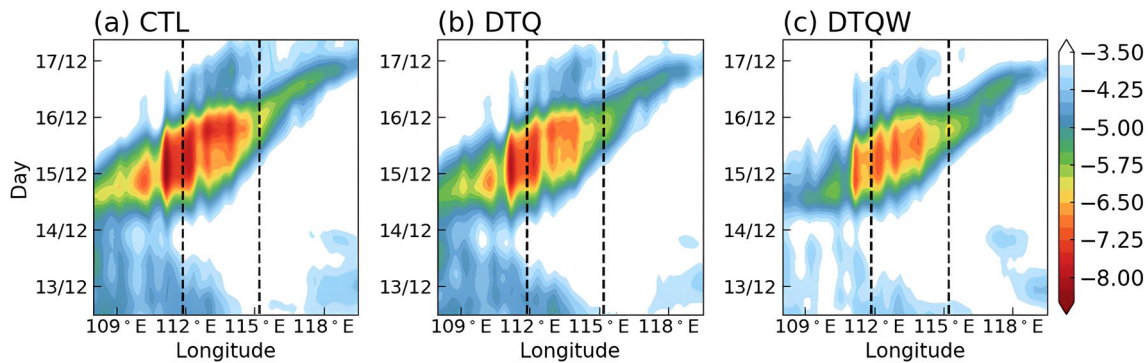


Fig. 16 Time-longitude cross-section of meridional gradients of the 850-hPa equivalent potential temperature (units: $\text{K } 100 \text{ km}^{-1}$) averaged between 21.5° N – 24.2° N in the **a** CTL, **b** DTQ and **c** DTQW

runs, respectively. The black dashed lines outline the meridional boundaries of the PRD region. See text for more details

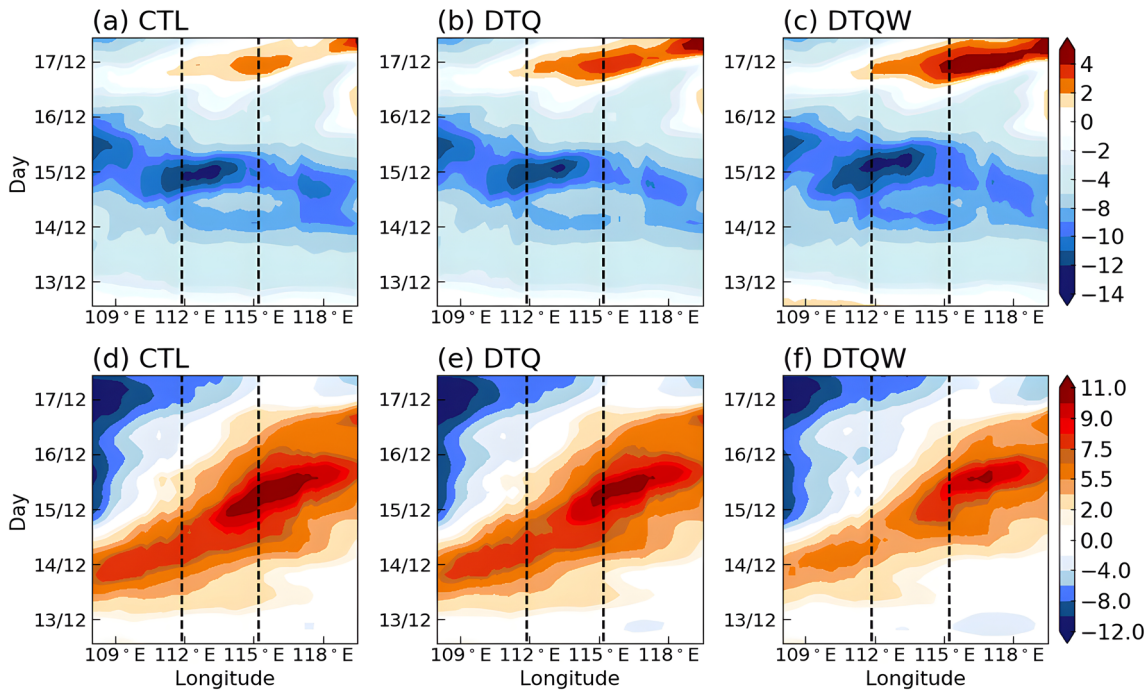


Fig. 17 Same as Fig. 16, but for the 850-hPa **a–c** zonal and **d–f** meridional winds (units: m s^{-1})

Negative values in Fig. 17a–c indicate a strong easterly wind, and positive values in Fig. 17d–f denote a southerly wind. As seen in CTL (Fig. 17a, d), low-level southeasterlies dominated PRD from December 13 to 16, before shifting to northwesterly winds once the cold front arrived on December 17; meanwhile, southerlies increased with time. 850-hPa low-level jets with wind speed excessing 10 m s^{-1} were found on December 15, with southerlies over eastern PRD and easterlies over western PRD corresponding to precipitation centers (see also Fig. 7a). Compared with CTL, there is no significant change in the low-level wind pattern in DTQ, except with slightly weaker jets (Fig. 17b, e). However in DTQW, the easterly jets appear to be more vigorous but with weaker southerlies (Fig. 17c, f). In other words, human activities induced an anomalous southwesterly over PRD during peak rainfall days in the CTL experiment.

Figure 18 presents the frequency distribution of the difference in 500-hPa vertical velocity in PRD between CTL and two perturbed runs, so as to indicate the intensity of vertical motions (Emori and Brown 2005). Relative to DTQ, stronger ascending motion, i.e., smaller than -0.6 Pa s^{-1} , tends to occur more frequently in CTL, while both weaker ascents and descents ($<\pm 0.6 \text{ Pa s}^{-1}$) become less frequent (blue line in Fig. 18). It suggests that human-induced thermodynamic effects on rainfall increase can be attributed to the more frequent occurrence of those stronger ascents. Note that frequency changes in CTL–DTQW are characterized by stronger probability in upward (and less downward) motion (see red line in Fig. 18). In fact, the frequency of upward motion changes displays a bimodal distribution with a primary peak at relatively weaker ascents of -0.45 Pa s^{-1} and a minor peak at stronger ascents of -1.2 Pa s^{-1} , echoing the rainfall frequency changes in CTL–DTQW (see blue line in Fig. 9).

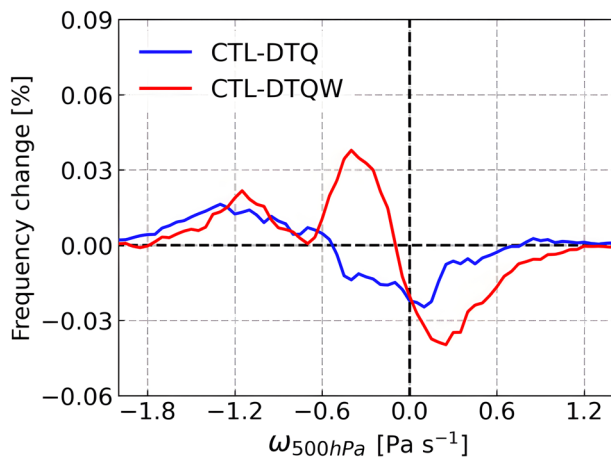


Fig. 18 Differences in the frequency of 500-hPa vertical velocity (units: Pa s^{-1}) over PRD for December 14–17, between CTL and DTQ (blue line), CTL and DTQW (red line)

Finally, we conducted moisture budget analyses to quantify thermodynamic and dynamic contributions to induced precipitation anomalies. Figure 19 presents the daily precipitation, 1000–100 hPa vertically integrated moisture fluxes and convergences (VIMFC), as well as thermodynamic and dynamic terms, for CTL minus the two perturbed runs. Both their spatial distribution (upper panels) and regional mean (bottom panels) are shown. As expected, the pattern of moisture flux convergence greatly resembles that of the precipitation anomaly, for both perturbed runs (Fig. 19a, b, e, f). It means that the moisture flux convergence change can be useful in explaining human-induced rainfall anomalies, such as the intensified southwest-northeast rainband and lower rainfall along the rainband's edges. Note that enhanced northward moisture transport in CTL–DTQW supports a further increase in precipitation, in relation to anomalous southerly winds (see vectors in Fig. 19f). Here the moisture flux convergence is decomposed into two terms: a thermodynamic term, i.e., $-\int \nabla \cdot (\vec{V}_{\text{CTL}} \delta q) dP$, determined by the specific humidity (q) anomaly, and a dynamic term, i.e., $-\int \nabla \cdot (q_{\text{CTL}} \delta \vec{V}) dP$, dictated by horizontal wind (\vec{V}) anomalies. For the thermodynamic term, its pattern is overall similar to the VIMFC anomaly pattern in CTL–DTQ, albeit with slightly reduced amplitudes, while in CTL–DTQW it contributes little or even negatively to VIMFC change over the southeastern coast (Fig. 19c, g). Further analysis indicates that the anomalous moisture increase over eastern SC (east of 114° E) was mainly due to the low-level flow (below 750 hPa), where easterlies dominate in CTL, transporting moisture to the west (rainband area) and drying the east, resulting in a negative contribution; in contrast, human-caused moisture increase in the west extended from the surface up to higher altitudes ($\sim 600 \text{ hPa}$) accompanied with southwesterly in CTL, resulting in positive outcomes (figures not shown). Also, CTL–DTQ shows the largest wind circulation-related dynamic contribution to VIMFC increases that occurred over the northwestern corner of PRD and Zhanjiang city ($110.5^\circ \text{ E}, 21.5^\circ \text{ N}$) (Fig. 19d). By comparing, the dynamic term in CTL–DTQW is highly consistent with the anomalous VIMFC and has a comparable magnitude to precipitation variations (Fig. 19h).

The bottom panels in Fig. 19 compare PRD-averaged moisture flux convergence changes and thermodynamic, dynamic terms for simulations from the six-member ensemble mean (bars) and individual members (error bars). The domain mean in CTL–DTQ shows that both dynamic and thermodynamic terms contributed equally to the overall enhancement in moisture flux convergence under human-induced warmer and wetter climates (Fig. 19i). Moreover, while individual members of simulations show a good agreement in the thermodynamic term, the dynamic term exhibits a relatively large variation

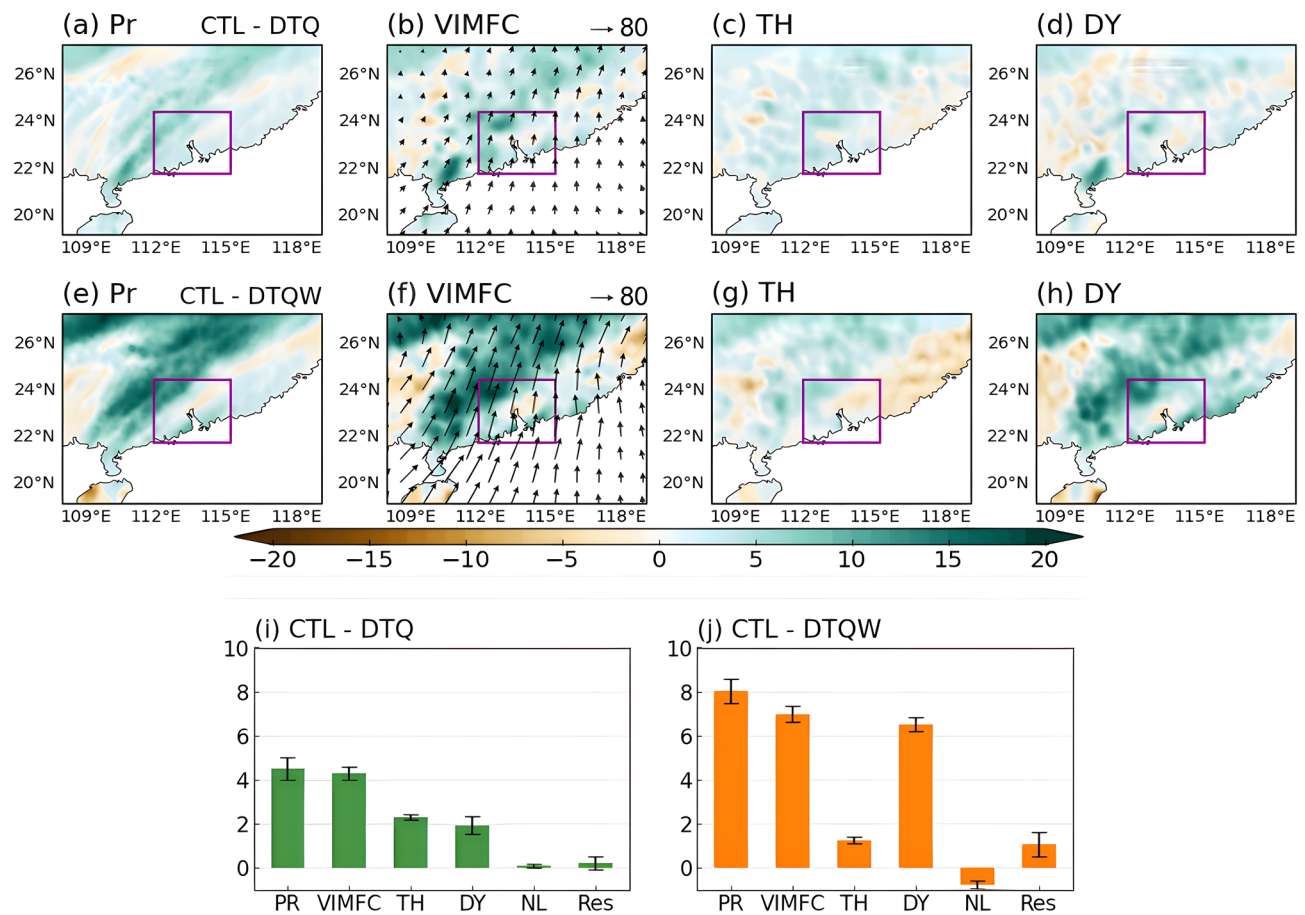


Fig. 19 Differences between **a–d** CTL and DTQ, **e–h** CTL and DTQW in **a**, **e** 4-day mean precipitation (Pr), **b**, **f** 1000–100 hPa vertical-integrated moisture fluxes (vectors; see the scale at top right in units of $\text{kg m}^{-2} \text{s}^{-1}$) and convergences (VIMFC; shading), as well as the separated **c**, **g** thermodynamic (TH) and **d**, **h** dynamic (DY) terms, averaged over the event period. Also shown are the regional-

averaged changes in PR, VIMFC, DY, TH, and a nonlinear term (NL, i.e., VIMFC-TH-DY) and residuals (Res, i.e., PR-VIMFC) that passed the 90% confidence level based on the Student's *t*-test, for **i** CTL-DTQ and **j** CTL-DTQW. All these terms are in units of mm per day for comparison. Purple boxes in the upper panels outline the PRD region

across different members, which is consistent with previous studies (Endo and Kitoh 2014; Lee et al. 2017). This implies that model uncertainty of dynamic processes associated with wind circulation changes can be the main contributor to uncertainty in estimating the moisture flux convergence. The CTL-DTQW domain-mean results confirm that the rainfall increase is mostly driven by the increase in the dynamic term, with a minor contribution from the moisture-related thermodynamic term (Fig. 19j), also reflecting previous works (e.g., Ali and Mishra 2018). The nonlinear term (NL) and biases (Res) between changes in precipitation and moisture flux convergence are much smaller than other terms and can be neglected (Lee et al. 2017; Seager et al. 2010; Lau and Kim 2015). More importantly, differences between the two perturbed runs suggest that the human-caused dynamic effects are critical to the additional increase in this extreme precipitation.

4 Conclusions and discussion

This study examines the sensitivity of an extraordinary precipitation event in winter 2013 over PRD to human influence using the convection-permitting WRF model and explored the underlying mechanisms for such impacts. Based on a multi-physics ensemble, the WRF model can well reproduce the observed rainfall, in terms of its rainband location and evolution. Quantitative attribution analyses were performed by downscaling this event with a factual IBC, and counterfactual IBCs with human influences on thermodynamic as well as dynamic components removed.

Spatial patterns of 4-day mean precipitation illustrate that human activities could cause the intensity of rainfall center over the northwestern PRD to increase by 7–10% and 13–15% under a 1.2 K warming due to human-caused thermodynamic forcing only and a 2 K warming due to the combined forcing of thermodynamic and dynamic components.

The frequency of rainfall changes with temperature peaks at $10\% \text{ K}^{-1}$ under thermodynamic forcing, whereas it shows a bimodal distribution peaking at $10\% \text{ K}^{-1}$ and $36\% \text{ K}^{-1}$ under the combined forcing. Moreover, we assessed the sensitivity of mean and extreme precipitation to human influences separately, and found that thermodynamic forcing alone has enhanced rain rates by 11% and 13% for the mean and extremes, respectively; the combined forcing has led to larger increases of 17% and 19% (21%) in the mean and 95th (99th) percentile, respectively. Based on these findings, we conclude that human-induced dynamic changes can accelerate the thermodynamic-driven rainfall increase in this event; daily mean rainfall changes are roughly consistent with the CC scaling of $\sim 7\% \text{ K}^{-1}$, whereas extreme rainfall increases can reach nearly a super-CC rate.

The underlying mechanisms for human-induced rainfall changes are summarized here: (1) Under human-related thermodynamic forcing, low-level thermal contrast exists between the SCS and the China continents, facilitating northward moisture transport and increasing cold-front intensity over PRD. Together with the help of low-level convergences and stronger updrafts, the rainfall increased as a result; (2) Under the combined forcing, thermal contrasts tend to be more noticeable, which favors anomalous southerly winds in PRD and thus dramatically strengthens the low-level wind convergence. The anomalous wind pattern in turn intensified the front system and ascending motions, resulting in a higher amplitude of rainfall change compared to thermodynamic-forced changes only. Moisture budget analysis suggests that thermodynamic component due to humidity changes and dynamic component due to wind circulation changes contribute equally to 4-day mean rainfall increases. On the other hand, the wind-related dynamic contribution mostly accounts for extreme rainfall changes, with humidity-related thermodynamic contribution being limited and negligible.

It is noteworthy that, as inferred from the comparison of two counterfactual runs, moisture amount can also be altered by circulation changes owing to global warming. In fact, based on moisture budget analyses, a sizable fraction of the PRD extreme rainfall exacerbation is due to dynamic effects, consistent with the results of SC rainfall using CESM (Li et al. 2019). However, there are also studies showing negative dynamic contributions to the tropical rainfall extremes based on CMIP3 outputs (Chou and Lan 2012). These previous results indicate the spatial spread of dynamic effects, which might be also related to the global model bias, limited sample size, and different methods for extracting human-induced warming signals. Thus, more examinations of dynamic effects on regional extreme rainfall are necessary. Besides, a shortcoming of the method for generating counterfactual conditions in WRF is that we assume human-caused perturbations to

remain constant over a month and remove the monthly mean from 6-hourly LBCs in WRF. While this assumption is plausible for anthropogenic warming with relatively small changes measured at that scale, it may introduce errors for more variable parameters (such as the winds) caused by human influences. More studies are needed to further fine-tune this method. In addition, this attribution analyses were conducted using CMIP5 models. However, attributions using CMIP6 are indeed worth undertaking as it outperforms CMIP5 in many aspects, albeit with little differences between historical temperature trends over SC from CMIP5 and from CMIP6. We plan to extend this study with the use of latest available CMIP6 model datasets.

The magnitude of extreme rainfall responses to human activities differs from case to case. Our results indicate that anthropogenic warming has intensified this wintertime rainstorm by 17%, with an interquartile range of 15–20%; Wang et al. (2018) concluded that it contributed to the 2017 Hurricane Harvey's extreme rainfall by about 20%, with a range of 13–37%. Multiple factors including differences in the model's ability to simulate rainfall, attribution methods, and thresholds for extreme rainfall identification as well as weather systems might have contributed to this discrepancy, however, a detailed discussion is beyond the scope of this study. More research on quantitatively examining human impacts on extreme precipitation in China is in urgent need.

Supplementary Information The online version contains supplementary material available at <https://doi.org/10.1007/s00382-023-06869-6>.

Acknowledgements The authors acknowledge the financial support from the General Research Fund of the Hong Kong Research Grants Council (14308017). We thank two anonymous reviewers for their constructive comments and suggestions.

Author contributions The study was designed by RZ and C-YT. RZ was responsible for data processing and analyses. RZ and C-YT were responsible for the model experiment design. The first draft of the manuscript was written by RZ and all authors commented on previous versions of the manuscript.

Funding This work was supported by the General Research Fund of the Hong Kong Research Grants Council (Grant 14308017).

Data availability The CPC rainfall data were obtained from (<https://psl.noaa.gov/data/gridded/>). The TRMM 3B42V7 data is obtained via the Goddard Earth Sciences Data and Information Services Center (<https://disc.gsfc.nasa.gov>). The ERA-Interim reanalysis was obtained from the ECMWF public datasets web interface (<http://apps.ecmwf.int/datasets>). The CRU TS data was obtained from the Climatic Research Unit website (https://data.ceda.ac.uk/badc/cru/data/cru_ts/cru_ts_3.00). The HadISST data is obtained via the Met Office Hadley Centre (<https://www.metoffice.gov.uk/hadobs>).

Declarations

Conflict of interest The authors declare that they have no competing interests.

References

- Alexander LV et al (2006) Global observed changes in daily climate extremes of temperature and precipitation. *J Geophys Res Atmos.* <https://doi.org/10.1029/2005JD006290>
- Ali H, Mishra V (2018) Contributions of dynamic and thermodynamic scaling in subdaily precipitation extremes in India. *Geophys Res Lett.* <https://doi.org/10.1002/2018GL077065>
- Allen MR, Ingram WJ (2002) Constraints on future changes in climate and the hydrologic cycle. *Nature.* <https://doi.org/10.1038/nature01092>
- Bougeault P, Lacarrere P (1989) Parameterization of orography-induced turbulence in a mesobeta-scale model. *Mon Weather Rev.* [https://doi.org/10.1175/1520-0493\(1989\)117%3c1872:POOITI%3e2.0.CO;2](https://doi.org/10.1175/1520-0493(1989)117%3c1872:POOITI%3e2.0.CO;2)
- Burke C, Stott P, Sun Y, Ciavarella A (2016) Attribution of extreme rainfall in Southeast China during May 2015. *Bull Am Meteorol Soc.* <https://doi.org/10.1175/BAMS-D-16-0144.1>
- Chen Y, Li W, Jiang X, Zhai P, Luo Y (2021) Detectable intensification of hourly and daily scale precipitation extremes across eastern China. *J Clim.* <https://doi.org/10.1175/JCLI-D-20-0462.1>
- Chou C, Lan CW (2012) Changes in the annual range of precipitation under global warming. *J Clim.* <https://doi.org/10.1175/JCLI-D-11-00097.1>
- Dee DP et al (2011) The ERA-Interim reanalysis: Configuration and performance of the data assimilation system. *Q J R Meteorol Soc.* <https://doi.org/10.1002/qj.82>
- Duan W, He B, Nover D, Fan J, Yang G, Chen W, Meng H, Liu C (2016) Floods and associated socioeconomic damages in China over the last century. *Nat Hazards.* <https://doi.org/10.1007/s11069-016-2207-2>
- Emori S, Brown SJ (2005) Dynamic and thermodynamic changes in mean and extreme precipitation under changed climate. *Geophys Res Lett.* <https://doi.org/10.1029/2005GL023272>
- Endo H, Kitoh A (2014) Thermodynamic and dynamic effects on regional monsoon rainfall changes in a warmer climate. *Geophys Res Lett.* <https://doi.org/10.1002/2013GL059158>
- Fischer EM, Knutti R (2016) Observed heavy precipitation increase confirms theory and early models. *Nat Clim Change.* <https://doi.org/10.1038/nclimate3110>
- Frame DJ, Rosier SM, Noy I, Harrington LJ, Carey-Smith T, Sparrow SN, Stone DA, Dean SM (2020) Climate change attribution and the economic costs of extreme weather events: a study on damages from extreme rainfall and drought. *Clim Change.* <https://doi.org/10.1007/s10584-020-02729-y>
- Fu G, Yu J, Yu X, Ouyang R, Zhang Y, Wang P, Liu W, Min L (2013) Temporal variation of extreme rainfall events in China, 1961–2009. *J Hydrol (amst).* <https://doi.org/10.1016/j.jhydrol.2013.02.021>
- Fung KY, Tam C-Y, Lee TC, Wang Z (2021) Comparing the anthropogenic heat and global warming impacts on extreme precipitation in urbanized pearl river delta area based on dynamical downscaling. *J Geophys Res.* <https://doi.org/10.1029/2021JD035047>
- Grell GA, Dévényi D (2002) A generalized approach to parameterizing convection combining ensemble and data assimilation techniques. *Geophys Res Lett.* <https://doi.org/10.1029/2002GL015311>
- Hong S (2006) Hongandlim-JKMS-2006. *J Korean Meteorol Soc* 42:129
- Huang H, Winter JM, Osterberg EC, Horton RM, Beckage B (2017) Total and extreme precipitation changes over the Northeastern United States. *J Hydrometeorol.* <https://doi.org/10.1175/JHM-D-16-0195.1>
- Huang X, Wang D, Liu Y, Feng Z, Wang D (2018) Evaluation of extreme precipitation based on satellite retrievals over China. *Front Earth Sci.* <https://doi.org/10.1007/s11707-017-0643-2>
- Huang W et al (2019) A possible mechanism for the occurrence of wintertime extreme precipitation events over South China. *Clim Dyn.* <https://doi.org/10.1007/s00382-018-4262-8>
- Huffman GJ et al (2007) The TRMM Multisatellite Precipitation Analysis (TMPA): quasi-global, multiyear, combined-sensor precipitation estimates at fine scales. *J Hydrometeorol.* <https://doi.org/10.1175/JHM560.1>
- Iacono MJ, Delamere JS, Mlawer EJ, Shephard MW, Clough SA, Collins WD (2008) Radiative forcing by long-lived greenhouse gases: calculations with the AER radiative transfer models. *J Geophys Res Atmos.* <https://doi.org/10.1029/2008JD009944>
- Janjic ZI (1994) The step-mountain eta coordinate model: further developments of the convection, viscous sublayer, and turbulence closure schemes. *Mon Weather Rev.* [https://doi.org/10.1175/1520-0493\(1994\)122%3c0927:TSMECM%3e2.0.CO;2](https://doi.org/10.1175/1520-0493(1994)122%3c0927:TSMECM%3e2.0.CO;2)
- Kain JS, Kain J (2004) The Kain-Fritsch convective parameterization: an update. *J Appl Meteorol.* [https://doi.org/10.1175/1520-0450\(2004\)043%3c0170:TKCPAU%3e2.0.CO;2](https://doi.org/10.1175/1520-0450(2004)043%3c0170:TKCPAU%3e2.0.CO;2)
- Kim KY, Kim BS (2020) The effect of regional warming on the East Asian summer monsoon. *Clim Dyn.* <https://doi.org/10.1007/s00382-020-05169-7>
- Kirchmeier-Young MC, Zhang X (2020) Human influence has intensified extreme precipitation in North America. *Proc Natl Acad Sci USA.* <https://doi.org/10.1073/pnas.1921628117>
- Lau WKM, Kim KM (2015) Robust Hadley circulation changes and increasing global dryness due to CO₂ warming from CMIP5 model projections. *Proc Natl Acad Sci USA.* <https://doi.org/10.1073/pnas.1418682112>
- Lau WKM, Wu HT, Kim KM (2013) A canonical response of precipitation characteristics to global warming from CMIP5 models. *Geophys Res Lett.* <https://doi.org/10.1002/grl.50420>
- Lee D et al (2017) Thermodynamic and dynamic contributions to future changes in summer precipitation over Northeast Asia and Korea: a multi-RCM study. *Clim Dyn.* <https://doi.org/10.1007/s00382-017-3566-4>
- Lenderink G, van Meijgaard E (2008) Increase in hourly precipitation extremes beyond expectations from temperature changes. *Nat Geosci.* <https://doi.org/10.1038/ngeo262>
- Lenderink G, Mok HY, Lee TC, van Oldenborgh GJ (2011) Scaling and trends of hourly precipitation extremes in two different climate zones—Hong Kong and the Netherlands. *Hydrol Earth Syst Sci.* <https://doi.org/10.5194/hess-15-3033-2011>
- Lenderink G, Barbero R, Loriaux JM, Fowler HJ (2017) Super-Claußius–Clapeyron scaling of extreme hourly convective precipitation and its relation to large-scale atmospheric conditions. *J Clim.* <https://doi.org/10.1175/JCLI-D-16-0808.1>
- Li C, Sun J (2015) Role of the subtropical westerly jet waveguide in a southern China heavy rainstorm in December 2013. *Adv Atmos Sci.* <https://doi.org/10.1007/s00376-014-4099-y>
- Li H, Chen H, Wang H (2017) Effects of anthropogenic activity emerging as intensified extreme precipitation over China. *J Geophys Res.* <https://doi.org/10.1002/2016JD026251>
- Li C et al (2018a) Attribution of extreme precipitation in the lower reaches of the Yangtze River during May 2016. *Environ Res Lett.* <https://doi.org/10.1088/1748-9326/aa9691>
- Li W, Jiang Z, Zhang X, Li L (2018b) On the emergence of anthropogenic signal in extreme precipitation change over China. *Geophys Res Lett.* <https://doi.org/10.1029/2018GL079133>
- Li P, Guo Z, Furtado K, Chen H, Li J, Milton S, Field PR, Zhou T (2019) Prediction of heavy precipitation in the eastern China flooding events of 2016: added value of convection-permitting simulations. *Q J R Meteorol Soc.* <https://doi.org/10.1002/qj.3621>
- Liu P, Tsimpidi AP, Hu Y, Stone B, Russell AG, Nenes A (2012) Differences between downscaling with spectral and grid

- nudging using WRF. *Atmos Chem Phys.* <https://doi.org/10.5194/acp-12-3601-2012>
- Liu C et al (2017) Continental-scale convection-permitting modeling of the current and future climate of North America. *Clim Dyn.* <https://doi.org/10.1007/s00382-016-3327-9>
- Lu C, Lott FC, Sun Y, Stott PA, Christidis N (2021) Detectable anthropogenic influence on changes in summer precipitation in China. *J Clim.* <https://doi.org/10.1175/JCLI-D-19-0611>
- Ma S, Zhou T, Dai A, Han Z (2015) Observed changes in the distributions of daily precipitation frequency and amount over China from 1960 to 2013. *J Clim.* <https://doi.org/10.1175/JCLI-D-15-0011>
- Ma Y, Yang Y, Mai X, Qiu C, Long X, Wang C (2016) Comparison of analysis and spectral nudging techniques for dynamical downscaling with the WRF model over China. *Adv Meteorol.* <https://doi.org/10.1155/2016/4761513>
- Min SK, Zhang X, Zwiers FW, Hegerl GC (2011) Human contribution to more-intense precipitation extremes. *Nature.* <https://doi.org/10.1038/nature09763>
- Myhre G et al (2019) Frequency of extreme precipitation increases extensively with event rareness under global warming. *Sci Rep.* <https://doi.org/10.1038/s41598-019-52277-4>
- Nie J, Sobel AH, Shaevitz DA, Wang S (2018) Dynamic amplification of extreme precipitation sensitivity. *Proc Natl Acad Sci USA.* <https://doi.org/10.1073/pnas.1800357115>
- Norris J, Chen G, David Neelin J (2019) Thermodynamic versus dynamic controls on extreme precipitation in a warming climate from the Community Earth System Model Large Ensemble. *J Clim.* <https://doi.org/10.1175/JCLI-D-18-0302.1>
- Pall P, Aina T, Stone DA, Stott PA, Nozawa T, Hilberts AGJ, Lohmann D, Allen MR (2011) Anthropogenic greenhouse gas contribution to flood risk in England and Wales in autumn 2000. *Nature.* <https://doi.org/10.1038/nature09762>
- Pfahl S, O'Gorman PA, Fischer EM (2017) Understanding the regional pattern of projected future changes in extreme precipitation. *Nat Clim Change.* <https://doi.org/10.1038/nclimate3287>
- Santer BD et al (2007) Identification of human-induced changes in atmospheric moisture content. *Proc Natl Acad Sci USA.* <https://doi.org/10.1073/pnas.0702872104>
- Seager R, Naik N, Vecchi GA (2010) Thermodynamic and dynamic mechanisms for large-scale changes in the hydrological cycle in response to global warming. *J Clim.* <https://doi.org/10.1175/2010JCLI3655.1>
- Shen Y, Xiong A (2016) Validation and comparison of a new gauge-based precipitation analysis over mainland China. *Int J Climatol.* <https://doi.org/10.1002/joc.4341>
- Shepherd TG (2014) Atmospheric circulation as a source of uncertainty in climate change projections. *Nat Geosci.* <https://doi.org/10.1038/NGEO2253>
- Skamarock WC et al (2008) A description of the advanced research WRF version 3, NCAR Tech. Note, NCAR/TN-468+STR. Natl. Cent. for Atmos. Res., Boulder
- Sun JQ, Ao J (2013) Changes in precipitation and extreme precipitation in a warming environment in China. *Chin Sci Bull.* <https://doi.org/10.1007/s11434-012-5542-z>
- Tabari H, Madani K, Willems P (2020) The contribution of anthropogenic influence to more anomalous extreme precipitation in Europe. *Environ Res Lett.* <https://doi.org/10.1088/1748-9326/abb268>
- Tewari M et al (2004) Implementation and verification of the unified NOAH land surface model in the WRF model. *Bull Am Meteorol Soc* 84:89–95
- Thompson G, Field PR, Rasmussen RM, Hall WD (2008) Explicit forecasts of winter precipitation using an improved bulk microphysics scheme. Part II: implementation of a new snow parameterization. *Mon Weather Rev.* <https://doi.org/10.1175/2008MWR2387.1>
- Trenberth KE, Zhang Y (2018) How often does it really rain? *Bull Am Meteorol Soc.* <https://doi.org/10.1175/BAMS-D-17-0107.1>
- Trenberth KE, Fasullo JT, Shepherd TG (2015) Attribution of climate extreme events. *Nat Clim Change.* <https://doi.org/10.1038/nclimate2657>
- van Oldenborgh GJ et al (2018) Corrigendum: attribution of extreme rainfall from Hurricane Harvey, August 2017. *Environ Res Lett* 12:124009. <https://doi.org/10.1088/1748-9326/aaa343>
- Wang SYS, Zhao L, Yoon JH, Klotzbach P, Gillies RR (2018) Quantitative attribution of climate effects on Hurricane Harvey's extreme rainfall in Texas. *Environ Res Lett.* <https://doi.org/10.1088/1748-9326/aabb85>
- Westra S et al (2014) Future changes to the intensity and frequency of short-duration extreme rainfall. *Rev Geophys.* <https://doi.org/10.1002/2014RG000464>
- Zhang W, Zhou T (2019) Significant increases in extreme precipitation and the associations with global warming over the global land monsoon regions. *J Clim.* <https://doi.org/10.1175/JCLI-D-18-0662.1>
- Zhang X, Wan H, Zwiers FW, Hegerl GC, Min SK (2013) Attributing intensification of precipitation extremes to human influence. *Geophys Res Lett.* <https://doi.org/10.1002/grl.51010>
- Zhong S, Qian Y, Zhao C, Leung R, Wang H, Yang B, Fan J, Yan H, Yang X-Q, Liu D (2017) Urbanization-induced urban heat island and aerosol effects on climate extremes in the Yangtze River Delta region of China. *Atmos Chem Phys* 17:5439–5457. <https://doi.org/10.5194/acp-17-5439-2017>
- Zhao R, Tam C-Y, Lee SM (2022) Attributing extreme precipitation characteristics in South China Pearl River Delta region to anthropogenic influences based on pseudo global warming. *J Clim (submitted)*

Publisher's Note Springer Nature remains neutral with regard to jurisdictional claims in published maps and institutional affiliations.

Springer Nature or its licensor (e.g. a society or other partner) holds exclusive rights to this article under a publishing agreement with the author(s) or other rightsholder(s); author self-archiving of the accepted manuscript version of this article is solely governed by the terms of such publishing agreement and applicable law.